# A new Single Crystal Growth of O-phenylene Diamine Dihydrochloride as a Polychloride: Optical and Electrical Properties of Thin Film


## Abstract

Single crystal organic compounds are perfectly suitable for elite organic field-effect transistors (OFETs) because of their arranged atomic pressing and smooth surface. Crystals of o-phenylenediamine dihydrochloride, $C_6H_4(NH_2)_2.2HCl$ $[OPDDH]^c$ is magnificently synthesized in a highly acidic medium; crystal structure is determined as monoclinic, space group C2/c, with a=7.324(2), b= 14.497 (5), c=7.992(3)Å, $\alpha$= 90, $\beta$= 94.04(4) and $\gamma$ = 90 (°), V = 846.4(5) $Å^3$ and Z=4. The different interactions in the crystal are investigated by Hirshfeld surface analysis. The geometry, highest occupied molecular orbital (HOMO), lowest unoccupied molecular orbital (LUMO) and other active parameters are calculated by density functional theory (DFT) on Material Studio 7.0. Nanostructured thin film of $[OPDDH]^c$ is fabricated by spin coating method. The single crystal and nanostructured thin film of $[OPDDH]^c$ are characterized by various techniques including UV–Vis–NIR, and single & powder X-ray diffraction. The refractive parameter dispersion and dielectric constants of $[OPDDH]^c$ are examined by Wemple–DiDomenico and single Sellmeier oscillator models. The optical parameters indicate that the $[OPDDH]^c$ thin film has a comparatively high absorption zone within 2-6 eV of photon energy range. The activation energies ($E_a$) and Urbach energy ($E_U$) of $[OPDDH]^c$ thin film are found to be 2.01 and 0.378 eV, respectively. The acquired results indicate that the $[OPDDH]^c$ thin film is a good candidate as a solar cell based on its dispersion parameters and band gap.



**Keywords:** Polychloride; Thin film; Hirshfeld surface analysis; DFT calculations; Optical and electrical properties.


## 1. Introduction

Major efforts have been concentrated on the design and enhancement of highly efficient semi-organic nonlinear optical (NLO) materials [1-3]. Harmonics generation, optical parametric oscillation and optical limiting are among their promising applications in photonics. The movement of delocalized π-electron cloud from donor to acceptor in a phenyl ring can be produced in various nonlinear optical compounds [4]. On the other hand, inorganic molecules have nonlinear optical properties lower than organic molecules because of their fast-nonlinear response through a wide frequency range. The advantages of an organic substances are rapid nonlinear response, adaptability in synthesis, minimal effort, and scope for fluctuating the properties by substitution of the function groups. The π–electron system interfacing the donor/acceptor groups (D/A) in organic molecules in exceedingly polarizable substances may upgrade utilizing organic crystals for NLO

in various applications [5,6]. For integrated optics, the construction techniques of organic nonlinear optical crystalline films within the range thickness of 0.2- 10 µm was reported [7]. O-phenylenediamine dihydrochloride single crystal is constructed by chloride cations and anions with $C_6H_4(NH_3)_2^{2+}$ through the hydrogen bonding network. O-phenylenediamine dihydrochloride crystal structure has four unique distances of (C-C) in the chemical structure as the protonated molecule in crystal structure of C2 symmetry type. The chloride anions are sited between the sequences layers and joined to three cations and through hydrogen bonds N-H-Cl forming polyhalides linkages [1-5,8]. These compounds come from aromatic amines as the o-phenylene diamine that forms many complexes with chlorine, bromine and iodine at various mole ratios and with different crystal systems [9-12]. The work objectives are arranged not just to improve the execution of organic materials for conceivable incorporation in devices, but additionally to satisfy the pressing requirement for knowledge into the applicable physical procedures that oversee the charge transport through these materials. This accentuates the significance of the control of imperfections and impurity states in organic molecular crystal with a specific end goal to achieve the desired photoelectrical properties. In this present work, o-phenylenediamine dihydrochloride single crystal as a polyhalide was successfully prepared in aqueous highly acidic medium. The hydrogen concentration of the crystal growth medium adjusted by concentrated HCl, reached pH≅ 0.5. Thin film from o-phenylenediamine dihydrochloride single crystal was fabricated by spin coating. The optical properties of the obtained nanostructured thin film were also studied.

## 2. Experimental

### 2.1. Raw materials

All involved chemicals were used without further purification. O-phenylene diamine $C_6H_4(NH_2)_2$ (Sigma-Aldrich) was used as purchased. Hydrochloric acid, chromic acid, ethanol, dimethyl formamide (DMF) and, sulfuric acid, isopropyl alcohol were obtained from Sigma-Aldrich.

### 2.2.Single crystals synthesis

Single crystals of $[OPDDH]^c$ were synthesized by dissolving o-phenylene diamine monomer in 50 ml absolute ethanol. The pH value of the resulting mixture was adjusted by addition of concentrated hydrochloric acid until reaching 0.5. The evaporation technique under room temperature was used to form the single crystal. The growth period of crystals was observed to be 25–32 days. The photograph of the $[OPDDH]^c$ crystals is shown in Fig. 1.

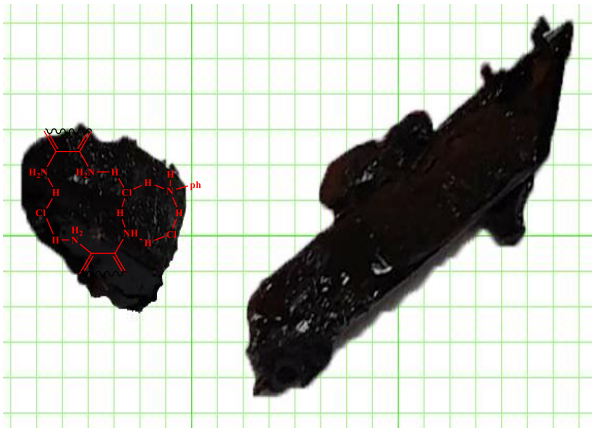

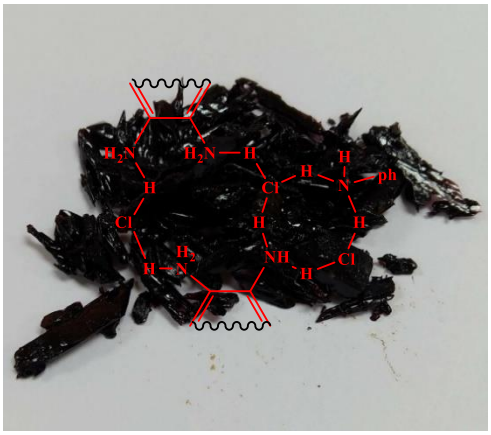

Fig. 1: Grown single crystals of o-phenylenediamine dichloride [OPDDH]$^{c}$

### 2.3. Fabrication of [OPDDH]$^{c}$ as-deposited thin film

o-phenylenediamine dichloride [OPDDH]$^{c}$ single crystal was dissolved in dimethyl formamide (DMF) at room temperature. Thin film was fabricated from solution by using spin coating (SPIN TC100) technique on clean glass and quartz substrate. The fabrication of the thin film was carried out through the two stages as follows:

**- Preparation of substrate before coating process**: The chromic acid is usually used for a purity made by adding concentrated sulfuric acid to a dichromate. Before the coating process, the quartz substrates were cleaned by chromic acid followed by ultra-sonication and then dried under nitrogen. The dry nitrogen gas was used to dry the substrates, followed by using atomic bombardment cleaning option in the first stage of supervises the evacuation process. The cleaned substrates were kept to use in the second stage (spin coating process).

**- Technological stage of spin coating process:** Different weights 0.5, 0.6 and 0.7 g of [OPDDH]$^{c}$ were dissolved individually in 70 ml in DMF at 65 $^{o}$C under magnetic stirrer (650 rpm). Cleaned optical quartz was deposited [OPDDH]$^{c}$ as thin film by using spin coating, with speed 2800 revs for 30 seconds. The resulting film was kept dry/48 h in an evacuated dictator for using and analyzing. The thickness of [OPDDH]$^{c}$ deposit films (≅ 250 ± 2 nm) was measured by M-2000 Ellipsometer.

### 2.4. Characterization of [OPDDH]$^{c}$

The following several techniques have been used including, X ray diffraction (XRD): Enraf-Nonius Mach3 diffractometer using λ(MoKα) = 0.71073 Å with SHELX-97 [13] in the WINGX software [14]; XPERT (PHILIPS) diffractometer unit, using Cu anode material at 40 kV and 25 mA with Kα: 1.541837 Å, UV–vis–NIR: Perkin Elmer (RSA-PE-20) spectrophotometer (4000-400) type instrument Lambda-35,

Excitation & Emission: Perkin–Elmer LS55 Fluorimeter using a 450 W xenon lamp as the excitation source, Electrical measurements: Keithley 6517B electrometer (8002A) for High Resistance Test Fixture; Keithley 2000 electrometer a 4-point test fixture equipped for Lower Resistivity, and Density Functional Theory (DFT): DMol$^3$ is available as part of Materials Studio. Copyright (c) 2013, Accelrys Inc. [15-16]

## 3. Results and discussion

### 3.1. Crystals of [OPDDH]$^c$

#### 3.1.1. Structure description:

All data concerning the measurements conditions, crystal data and final results of the structure determination are gathered in Table 1. The Oak Ridge Thermal Ellipsoid Plot Program (ORTEP) [17] drawing depicted in the Fig. 2, shows that the asymmetric unit of the crystal structure consists of three carbon atoms (C1, C2, C3), one nitrogen atom (N1), one chloride atom (Cl1) and five hydrogen atoms. All these atoms occupy general positions in the unit cell. Application of the symmetry completes the chemical formula ($C_6H_4(NH_3)_2Cl_2$) of the compound [OPDDH]$^c$. Atomic coordinates and geometric characteristics of this molecule are given in the Tables 2 and 3.

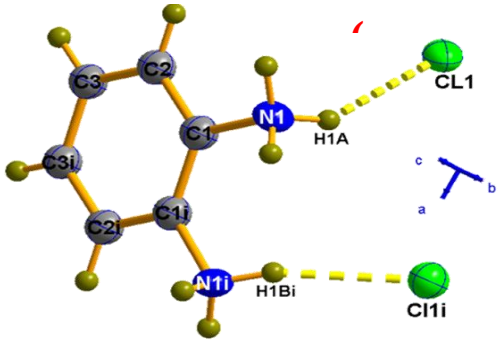


Fig. 2(a): ORTEP drawing of the formula unit drawn by thermal ellipsoids are drawn to enclose 50% probability

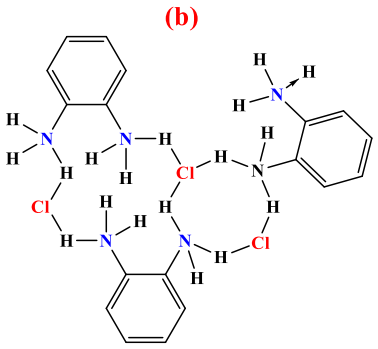


Fig.2(b): Structure of [OPDDH]$^c$ drawn by ChemDraw professional 15.0

Figure 3 shows a perspective view of the unit cell of [OPDDH]$^c$, which contains four of each ion o-$C_6H_4(NH_3^+)_2$ and $Cl^-$.

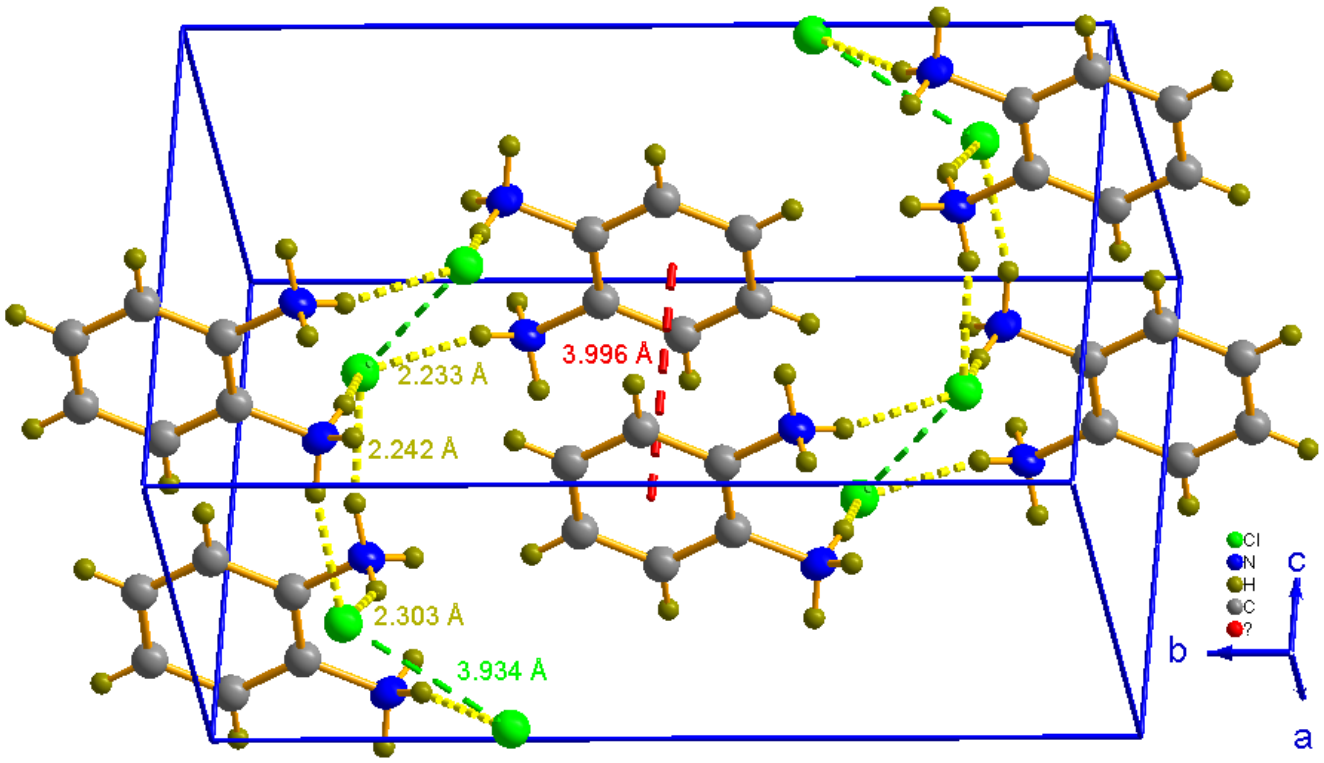


Fig. 3: Perspective view of the unit cell in the crystal structure of $[OPDDH]^{c}$.

This structure is not iso-structural with others o-phenylene diamine.2HX [10, 12], but it agrees with that reported by Claes Stalhandske [8] which shows that the $[OPDDH]^{c}$ can crystallize in two crystalline phases, one monoclinic (C2/c) and another orthorhombic (Pmmm). This could explain the existence in the PXRD pattern Fig. 4, of some lines that do not belong to the monoclinic phase but belong to the orthorhombic phase as impurity.

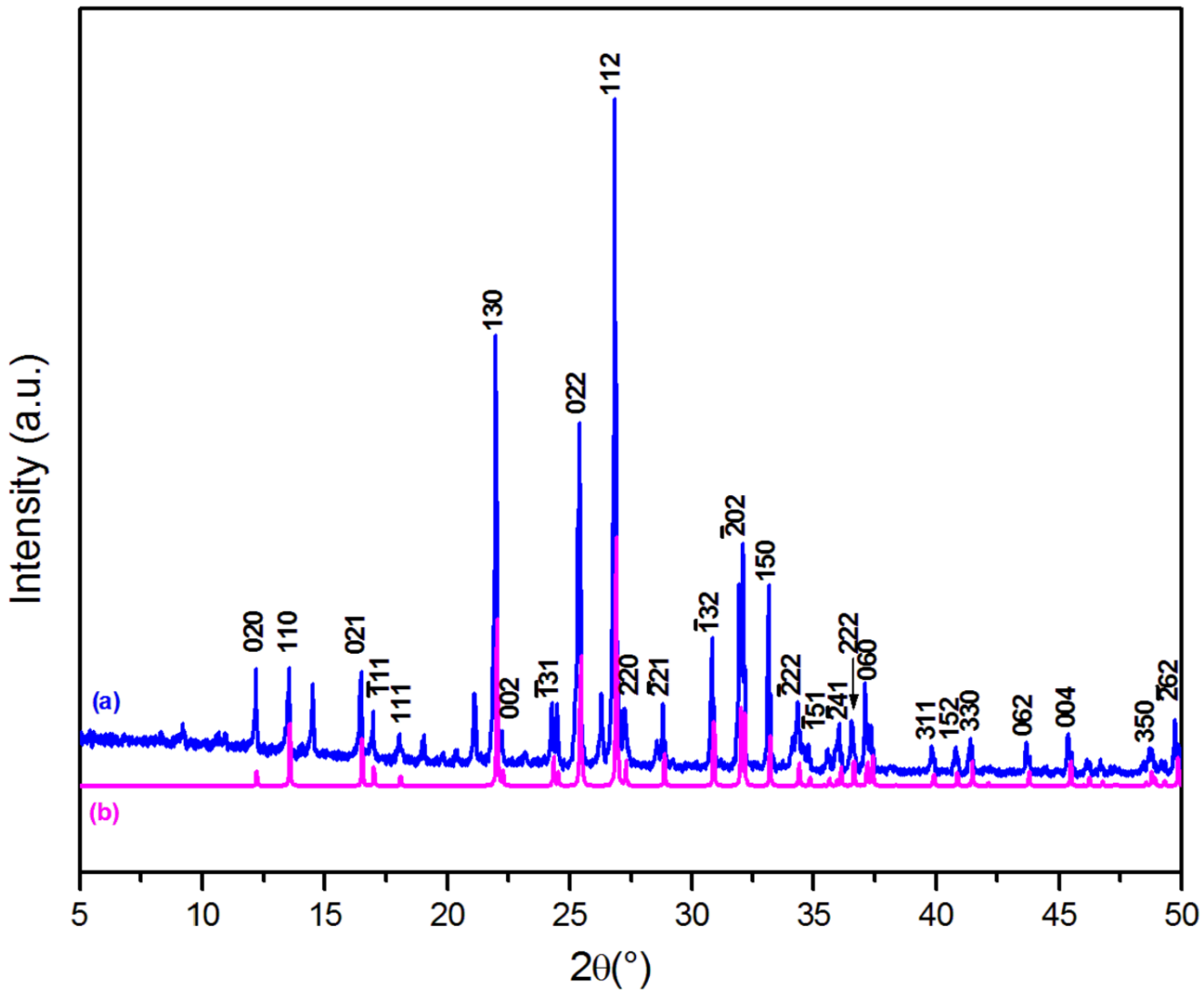


Fig. 4: Experimental (a) and simulated (b) powder X-ray diffraction patterns of [OPDDH]$^{c}$.

The chloride ions which are smaller than $Br^-$ and $I^-$ leave between o-$C_6H_4(NH_3^+)_2$ molecular planes a spacing of 3.9 Å, which creates different types of interactions (Fig. 3) between these entities, which we can identify mainly (H-bonds, Cl--Cl and π–π). The C-N length, 1.4542 Å, corresponds to the C-$NH^+$ bond length, found in the related compounds (l.450 - 1.501Å) [6-8, 10, 18]. Domenicano an al. [19] proposed that the 'standard' length of the aromatic C-$NH^+$ bond was 1.464 Å, which they calculated as the weighted mean value of 6 ring- substituted anilinium cations. For the non-protonated C-$NH_2$ bond, the reported lengths are significantly shorter than those of C-$NH^+$; namely, 1.351-1.391 Å [6, 18, 20]. Given these data concerning the C-N bond length, the amino group in [OPDDH]$^{c}$ is protonated. The nitrogen atom is surrounded by three chloride ions at Cl-N distances of 3.099(1), 3.104(2) and 3.106(2) Å. These values are lower than those found for N-I (3.46 - 4.06 Å) [21- 22] since Cl is smaller than I. The cations o-$C_6H_4(NH_3^+)_2$ are planar and parallel to the ab plane, except for the amino hydrogens (r.m.s. deviations ± 0.006 Å, with a dihedral angle of

N1—C1—C2—C3 equal to 177.9°). They develop with Cl- ions a three-dimensional network of hydrogen bonding (Table 4) which stabilizes the crystal packing of the title compound. The centroids of the aromatic rings of $[OPDDH]^c$ are separated by 3.996 Å which also develops π–π interactions. To complete the study of existing interactions, Analysis of Hirshfeld surfaces was performed.

Table 1. Crystal data, data collection and structure refinement details of $[OPDDH]^c$.

| ***Crystal data*** | | ***Data collection*** | |
|---|---|---|---|
| Chemical Formula | $C_6H_{10}N_2Cl_2$ | Enraf Nonius Mach III diffractometer | $R_{int}$ = 0.083 |
| $M_r$ = 181.06 | $D_x$ = 1.421 Mg m$^{-3}$ | Graphite monochromated (MoKa =0.71073Å). | $\theta_{max}$ = 28.0°, $\theta_{min}$ = 2.8° |
| Monoclinic, *C*2/*c* | Mo Kα radiation, λ = 0.71073 Å | non–profiled ω/2θ scans | *h* = −9 9<br>*k* = −2 19<br>*l* = −3 10 |
| *a* = 7.324 (2) Å | Cell parameters from 25 reflections | 1733 measured | |
| *b* = 14.497 (5) Å | θ = 9–11° | 1025 independent | 2 standard every 120 min |
| *c* = 7.992 (3) Å | μ = 0.70 mm$^{-1}$ | 966 reflections with $I > 2\sigma(I)$ | intensity decay: - 4% |
| β = 94.04 (4)° | *T* = 293 K | | |
| *V* = 846.4 (5) Å$^3$ | Prism, 0.30 × 0.20 × 0.10 mm$^3$ | | |

| ***Refinement*** | | | |
|---|---|---|---|
| Refinement on $F^2$ | Secondary atom site location: difference Fourier map | 1025 reflections | $\Delta\rho_{max}$ = 0.48 e Å$^{-3}$ |
| Least-squares matrix: full | Hydrogen site location: inferred from neighboring sites | 48 parameters | $\Delta\rho_{min}$ = −0.26 e Å$^{-3}$ |
| $R[F^2 > 2\sigma(F^2)]$ = 0.031 | H atoms treated by a mixture of independent and constrained refinement | 0 restraints | Extinction correction: SHELXL, $Fc^*=kFc[1+0.001xFc^2\lambda^3/\sin(2\theta)]^{-1/4}$ |
| $wR(F^2)$ = 0.083 | $w = 1/[\sigma^2(F_o^2) + (0.0416P)^2 + 0.2928P]$ where $P = (F_o^2 + 2F_c^2)/3$ | The a | Extinction coefficient: 0.104 (7) |
| *S* = 1.18 | $(\Delta/\sigma)_{max}$ = 0.001 | | |

Table 2: Coordinates of fractional atomic (x, y, z, $U_{iso}$*/$U_{eq}$) (Å)

| | *x* | *y* | *z* | *Uiso*/Ueq* |
|---|---|---|---|---|
| Cl1 | 0.02318 (4) | 0.67697 (2) | 0.49012 (4) | 0.03866 (19) |
| N1 | 0.31202 (15) | 0.66765 (7) | 0.79300 (14) | 0.0325 (3) |
| H1A | 0.2632 | 0.6861 | 0.6935 | 0.049* |
| H1B | 0.3891 | 0.7105 | 0.8353 | 0.049* |
| H1C | 0.2235 | 0.6590 | 0.8622 | 0.049* |
| C1 | 0.41045 (14) | 0.58164 (8) | 0.77350 (13) | 0.0277 (3) |
| C2 | 0.32197 (19) | 0.49919 (8) | 0.7980 (2) | 0.0398 (3) |
| H2 | 0.2024 | 0.4991 | 0.8302 | 0.048* |
| C3 | 0.4112 (2) | 0.41698 (9) | 0.7747 (2) | 0.0507 (4) |
| H3 | 0.3522 | 0.3614 | 0.7922 | 0.061* |

Table 3: Geometric parameters (Å, °)

| | | | |
|---|---|---|---|
| N1—C1 | 1.4542 (14) | C1—C1i | 1.390 (2) |
| N1—H1A | 0.8900 | C2—C3 | 1.3784 (19) |
| N1—H1B | 0.8900 | C2—H2 | 0.9300 |
| N1—H1C | 0.8900 | C3—C3i | 1.385 (3) |
| C1—C2 | 1.3801 (16) | C3—H3 | 0.9300 |
| C1—N1—H1A | 109.5 | C1i—C1—N1 | 120.90 (6) |
| C1—N1—H1B | 109.5 | C3—C2—C1 | 119.84 (12) |
| H1A—N1—H1B | 109.5 | C3—C2—H2 | 120.1 |
| C1—N1—H1C | 109.5 | C1—C2—H2 | 120.1 |
| H1A—N1—H1C | 109.5 | C2—C3—C3$^{i}$ | 120.15 (8) |
| H1B—N1—H1C | 109.5 | C2—C3—H3 | 119.9 |
| C2—C1—C1i | 120.00 (7) | C3i—C3—H3 | 119.9 |
| C2—C1—N1 | 119.08 (10) | | |
| C1i—C1—C2—C3 | −0.4 (2) | C1—C2—C3—C3$^{i}$ | −0.6 (3) |
| N1—C1—C2—C3 | 177.88 (13) | | |

Symmetry code: (i) −x+1, y, −z+3/2.

Table 4. Hydrogen-bond geometry (Å, °)

| *D*—H···*A* | *D*—H | H···*A* | *D*···*A* | *D*—H···*A* |
|---|---|---|---|---|
| N1—H1A···Cl1 | 0.89 | 2.31 | 3.1036 (18) | 148 |
| N1—H1B···Cl1$^{ii}$ | 0.89 | 2.23 | 3.0991 (14) | 164 |
| N1—H1C···Cl1$^{iii}$ | 0.89 | 2.24 | 3.1062 (16) | 164 |

Symmetry codes: (ii) *x*+1/2, −*y*+3/2, *z*+1/2; (iii) −*x*, *y*, −*z*+3/2.

### 3.2. Hirshfeld surface analysis

To quantify and visualize the different types of interactions in the crystal structure of [OPDDH]$^{c}$, we performed the Hirshfeld Surfaces (HS) analysis [23] using the Crystal Explorer 3.1 software [24].

Intermolecular interactions strengths and directions in the crystal construction were plotted onto HS using the regularized contact distance ($d_{norm}$) which is defined in terms of internal and external spaces de and di and the Van Der Waals (VDW) radii of atoms, and expressed as:

$d_{norm} = (d_i - r_i^{vdw})/r_i^{vdw} + (d_e - re^{vdw})$, where $r_i^{vdw}$ and $r_e^{vdw}$ are the VDW radii of the atoms [25].

Fig. 5(a) shows that HS of $[OPDDH]^c$ has been drawn over a $d_{norm}$ between -0.52 (red) and 1.07 Å (blue), which has been revealed as transparent to allow picturing of all the atoms around the molecule. The Full Plot (FP) displaying several crystal packing interactions in $[OPDDH]^c$ is revealed in Fig. 5(b). The concentrated hot spots (red colored) on the surface in relation to $d_{norm}$ relate to hydrogen bonds including the nitrogen and chlorine atoms with adjacent molecules Fig. 5(c).

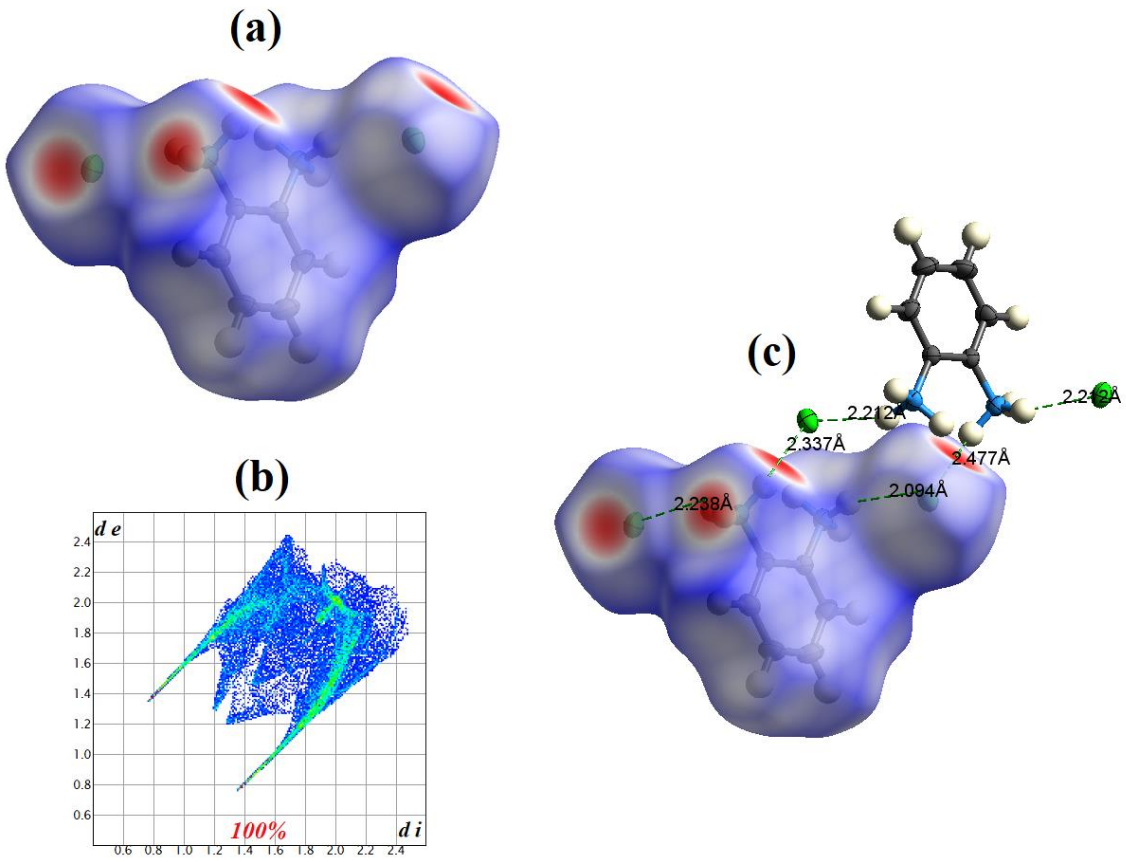


Fig. 5(a) Hirshfeld Surface mapped with $d_{norm}$ for $[OPDDH]^c$. (b) 2D Full plots of $[OPDDH]^c$ (c) HS mapped over $d_{norm}$ with the shortest contacts.

The interpretation of the FP (Fig. 6a & 6b) revealed that Cl…H / H…Cl contacts strongly (55%) to the total HS. The spike at (de + di) ~ 2, 1 Å in acceptor region of FP with a 33%, corresponds to Cl…H contacts. However, in the donor region, the FP plot matches a 22% contribution from H…Cl contacts to the HS. These Cl…H / H… Cl contacts form a hydrogen bonding 3D network in the crystal structure of [OPDDH]$^{c}$. This confirms the crucial role of chloride anions in the formation of the 3D supramolecular network evinced by the XRD investigation. The H…H interactions appeared in the 2D fingerprint map at the middle of scattered points, including 30.2% of the total Hirshfeld surfaces. This reveals that VDW interactions have a significant effect on the construction of the 3D geometry of [OPDDH]$^{c}$. Moreover, H···C/C···H excerpt is revealed as wings on the bottom right (C···H) and top left (H···C) of the 2D plot with 7.6% of the total surface. The proportions of C…C contacts deform 6.6% of the HS area.

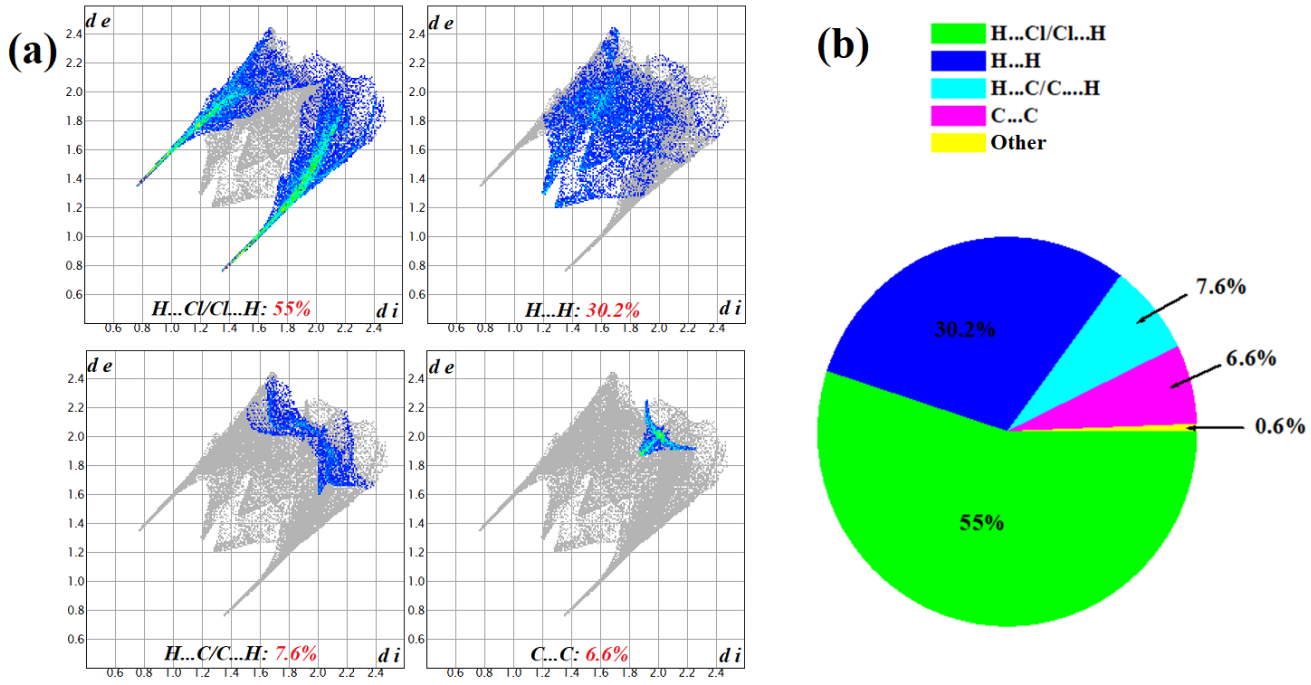


Fig. 6(a) 2D fingerprint plot; (b) The basis of HS analysis.

### 3.3. Global reactivity descriptors by using Density Functional Theory (DFT)

The theoretical description of chemical reactivity descriptors of [OPDDH]$^{c}$ as a polychloride, has benefited significantly from the development of density functional theory (DFT ) methods (scheme 1). In numerical applications of DFT, $E_{HOMO}$ and $E_{LUMO}$ are calculated through the following approximate versions of DMol$^{3}$, based upon the finite difference approximation. Table 5 shows global electrophilicity index (ω), hardness (η) and softness (S), for [OPDDH]$^{c}$ coming out from their theoretical description of chemical reactivity descriptors. The chemical potential (μ) of [OPDDH]$^{c}$ is interrelated to charge transfer from a

system of high (μ) to lower value of (μ). The normalization constraint in DFT, the numerical value of electronegativity (χ) has been identified as the negative of the chemical potential (μ) [26]. All these results are tabulated in Table 5. For nucleophilic attack and HOMO level, the most reactive site of $[OPDDH]^c$ occurs at N(7) and N(8) atoms of the amine functional group. A theoretical value for the energy ΔE of $[OPDDH]^c$ ΔE ≅ 4.314 eV was used to calculate the energy of electrons transferred betwwen HOMO and LUMO, ensuring good stability for $[OPDDH]^c$ compound. The electrophilicity index (*ω*) is the most interesting quantum chemical descriptor of the global electrophilic nature of a molecule within a relative scale. It determines the stability in energy when the system gains supplemental electronic charge.

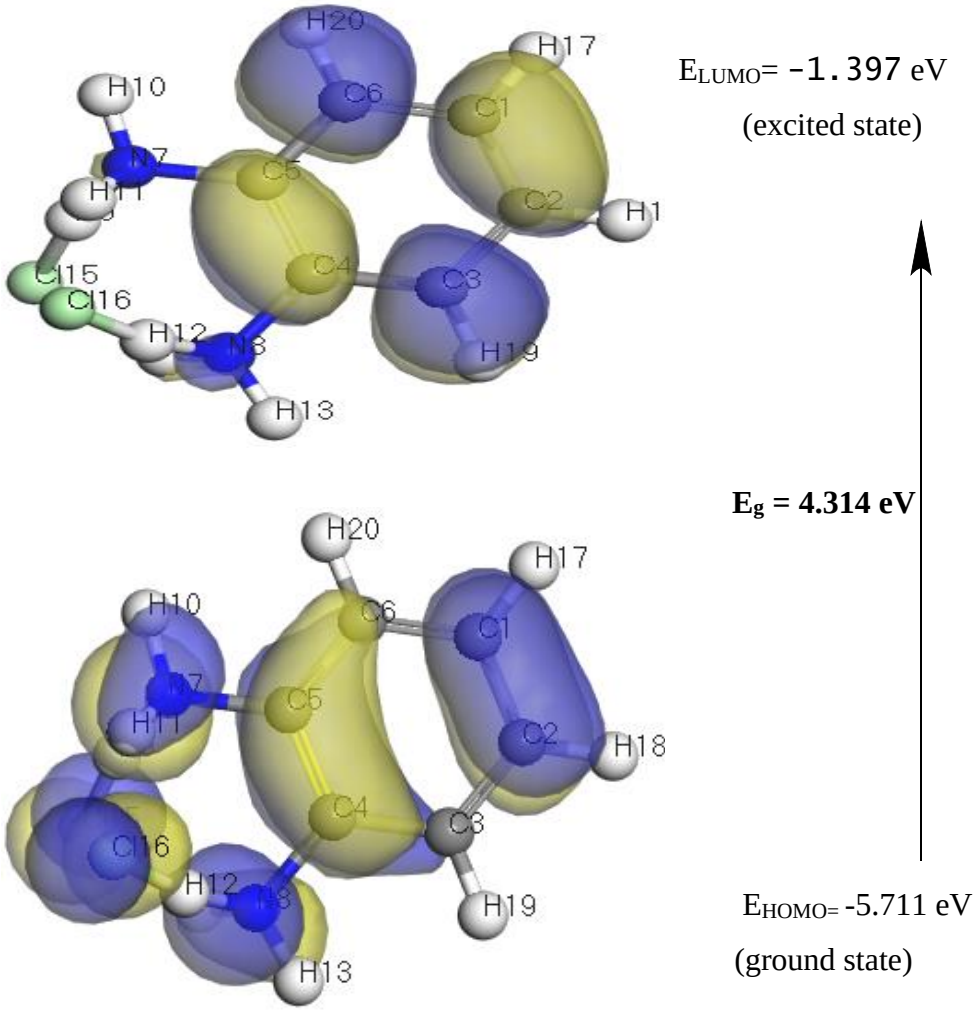


Scheme 1: 3D plots frontier orbital energies using DFT method for $[OPDDH]^c$.
Energy of Highest Occupied Molecular Orbital (EHOMO): -0.20989Ha, -5.711eV
Energy of Lowest Unoccupied Molecular Orbital (ELUMO): -0.05135Ha, -1.397eV

Table 5. EHOMO, ELUMO, electronegativity (χ), chemical potential (μ), global hardness (η), global softness (S), global electrophilicity index (ω) and softness (σ) for $[OPDDH]^c$ polychloride.

| Compound | EH | EL | (EH-EL) | χ(eV) | μ(eV) | η(eV) | S(eV) | ω (eV) | $DN_{max}$ | $\sigma(eV^{-1})$ |
|---|---|---|---|---|---|---|---|---|---|---|
| $[OPDDH]^c$ | -5.711 | -1.397 | -4.314 | 3.554 | -3.55 | 2.157 | 0.232 | 2.928 | 1.648 | 0.464 |

### 3.4. UV/Visble spectra measurements

The solid-state UV/Vis absorption spectrum (Fig. 7a-c) of $[OPDDH]^c$ consists of two bands, centered at 256 and 512 nm (5.17 eV and 2.59 eV). Quantum chemical calculation with DFT method at the B3LYP/6-31 +G* level was performed from the crystal data for the organic cation [o-$C_6H_4(NH_3^+)_2$], leading to LUMO and HOMO (Fig. 7(b)) between which the gap energy is Eg = 5.58 eV (238 nm). This allows attributing the observed band around 256 nm to the π-π transition that usually occurs in the UV field. The second absorption band of the spectrum of o-$C_6H_4(NH_3)_2Cl_2$, observed in the visible (around 512 nm) is due to exciton formed with the inorganic species $Cl^-$ [27]. From graphical representations, the energy band gap value (5.58 eV), which is estimated by Quantum chemical calculation with DFT method at the B3LYP/6-31+G*, is bigger in comparison to that (4.31 eV) estimated by DFT with DMol[3]

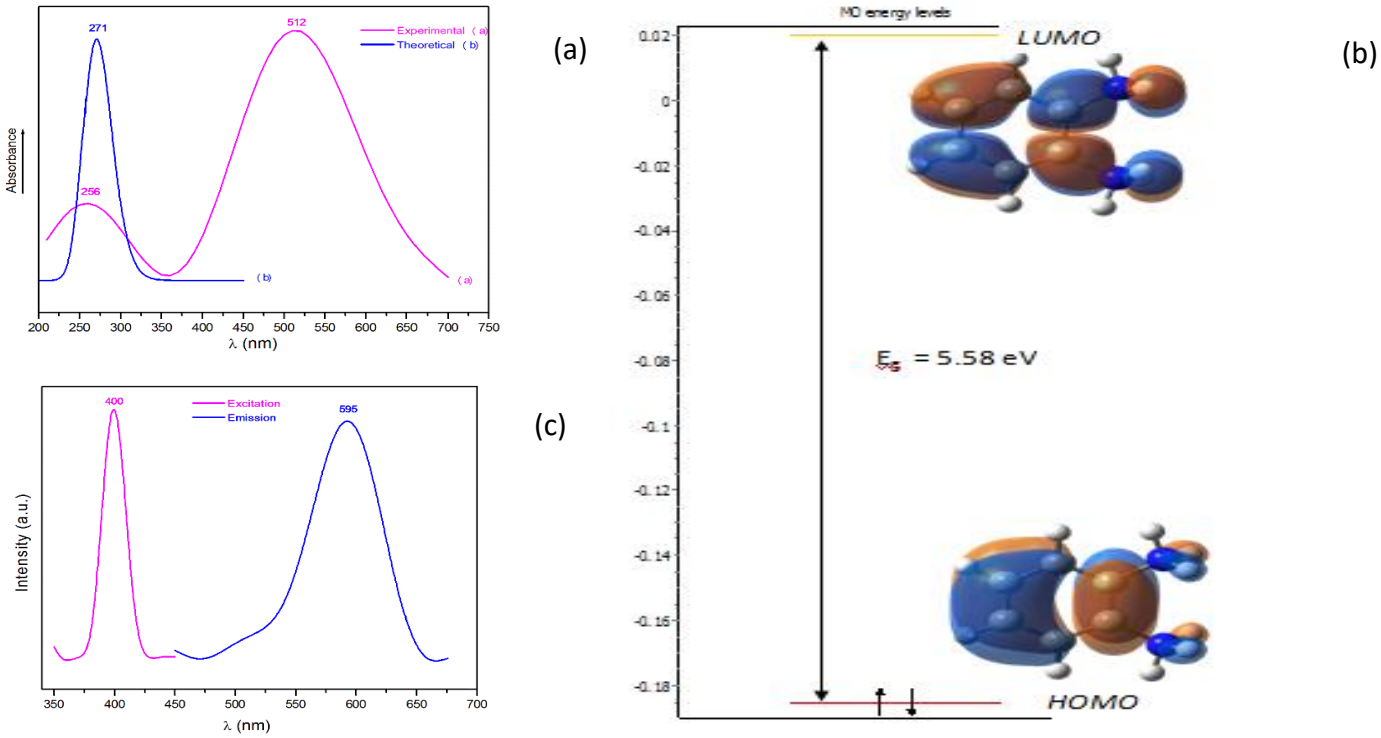


Fig. 7(a) Solid-state UV/Vis absorption spectrum of $[OPDDH]^c$
(b) Frontier molecular orbitals (HOMO and LUMO) of $[OPDDH]^c$.
(c) Solid state emission ($\lambda_{exc}$ = nm) and excitation ($\lambda_{emi}$ = nm) spectra of $[OPDDH]^c$.
The former is due to band gap absorption for the electronic transitions within the organic entity.

### 3.5. Optical band gap $E_g^{Opt}$

UV-visible diffuse reflectance spectroscopy (UV-V/DR) was used for the optical properties of [OPDDH]$^c$ to estimate its possible fabrication in polymer solar cells and optoelectronic devices [28]. The requirement of the UV-V/DR with photon energy (hν) of [OPDDH]$^c$ polychloride supports the estimation of the $E_g^{Opt}$ by the Tauc's formula and Kubelka-Munk (K-M) methods [29]. The properties calculated of $(F(R)h\nu)^2$ and $(F(R)h\nu)^{0.5}$ versus (h**ν**), of [OPDDH]$^c$ polychloride, are shown in Figs. (8a-8b).

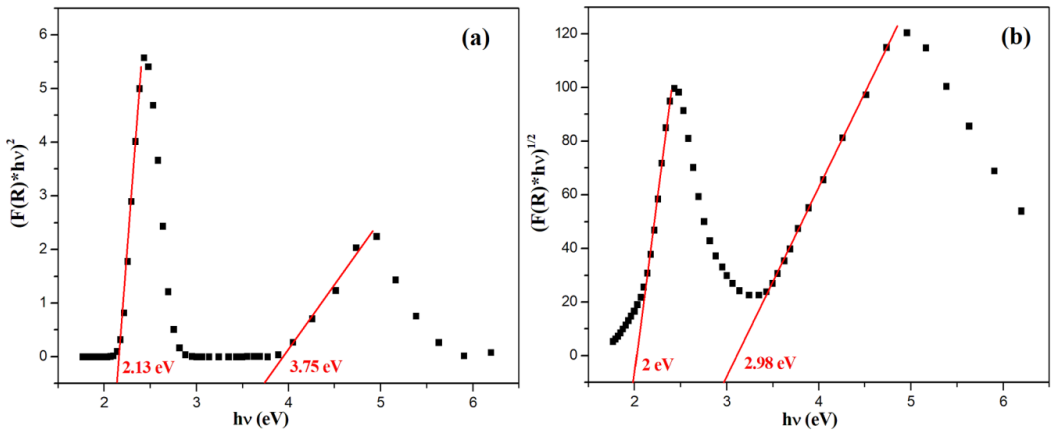


Fig. 8(a-b). UV-V/DR spectra of $E_g^{Opt}$ indirect **(a)** and direct (b) transition of [OPDDH]$^c$ polychloride.

The graphical investigation of the Eg, the noted UV-V/DR spectrum in the reflectance mode were transformed to an F(R) magnitude and plotted versus hν.The indirect band gap (IBG) and direct band gap (DBG) energy were determined by linear extrapolations of the straight lines to hν. It was found that the studied material, [OPDDH]$^c$, exhibits two band gaps; the estimated DBG values (2.13 and 3.75 eV) are higher than those of IBG (2 and 2.98 eV). This outcome is characteristic for a crystalline behavior of single crystal [30] and indicates that the tile material is a promising candidate for semiconductor device applications [31].

### 3.6. Nanostructured [OPDDH]c thin film

#### 3.6.1. Study by XRD

Fig. 10 shows the XRD patterns of [OPDDH]$^c$ at the room temperature. The single crystal is exhibiting a monoclinic that belongs to the space group C2/c. This pattern reveals that the obtained single crystal [OPDDH]$^c$ was enough to acquire fully [OPDDH]$^c$ as-deposited thin film. The lattice parameters (a, b, and c) for the monoclinic phase of single crystal [OPDDH]$^c$ were calculated [32] and their values are tabulated in Table 6. The calculated values, as well as the observed interplanar distances, d values, are in good agreement with the reported database_code_amcsd 0020049 [33]. The lattice parameters of monoclinic phase

of [OPDDH]$^{c}$ thin film were calculated from the peak position using the formulae of monoclinic system given by the following relation [34]:

$$\text{Monoclinic } d^{*2}(hkl) = \left(h^2a^{*2} + k^2b^{*2} + l^2c^{*2} + 2hla^*c^*(\cos\beta^*)\right)$$
$$d^2(hkl) = \left\{\frac{1}{\sin^2\beta}\left[\frac{h^2}{a^2} + \frac{l^2}{c^2} - \frac{2hl\cos\beta}{ac}\right] + \frac{k^2}{b^2}\right\}^{-1} \quad (1)$$

where d-spacing (d) and miller indices (hk*l*) are obtained from XRD data of the crystallographic planes shown in Fig. 10. The average crystallite size ($D_{av}$) was determined using Scherer's formula; $D_{av}=0.9\lambda/(FWHM)\cos\theta$, where $\lambda$ is the wavelength (1.5406 Å), $\theta$ is the Bragg angle ($D_{av} \cong 118.839$ nm) and FWHM is the full-width at half maximum. The crystallite size of the [OPDDH]$^{c}$ thin films increases with increasing of 2$\theta$, due to improvement in the density of nucleation centers in the [OPDDH]$^{c}$ thin films. The Peak position (2$\theta$), Miller indices (hk*l*), FWHM, d-spacing, the lattice strain ($\varepsilon$), the dislocation density ($\delta$) and the average inter-crystallite separation (S) of [OPDDH]$^{c}$ as-deposited thin film has been calculated. The lattice strain in powders can be expressed as: $\varepsilon = FWHM/4tan\theta$. From Table 6, the average of $\varepsilon$ is found to be 5.713 x $10^{-3}$. According to Scherrer's and the stain equations, the crystal size is indirectly proportional with cos ($\theta$). On the other hand, the strain is indirectly proportional to the tan ($\theta$). Thus, assuming that the $D_{av}$ and $\varepsilon$ equations are independent of each other and both have a Cauchy-like profile, the liner fit breadth is simply the sum of Scherrer's and stain contribution to line broadening equations [35].

$$FWHM = \frac{1.386}{D_{av}cos\theta} + 4\varepsilon sin\theta \quad \therefore \text{ FWHM}cos\theta = \frac{1.386}{D_{av}} + 4\varepsilon sin\theta \quad (2)$$

The above equations are Williamson-Hall methods; the strain and particles size can be determined from the slope and the intercept of the plot determined from the relation between (FWHM*cos$\theta$) and (4sin$\theta$) for [OPDDH]$^{c}$ as-deposited thin film, as shown in inset Fig.10. From the data, the crystalline size was estimated from the y-intercept (105.88 nm), and the strain $\varepsilon$ (6.3x$10^{-3}$), from the slope of the fit [36]. Where *f* is a factor equalling unity giving a minimum dislocation density, the dislocation density,$\delta$, of the films was determined by Williamson and Smallman's relation: $\delta = f/D^2$ [37]. The average inter-crystallite separation (S) of the [OPDDH]$^{c}$ as-deposited thin film was determined from the position of the maximum of the halo [38] $S = 7.7/8\sin\theta$. The average value of S is found to be 3.56 Å for [OPDDH]$^{c}$ as-deposited thin film. In comparison XRD pattern for single crystal (Fig. 4) with XRD pattern for thin film (Fig.10), it can be noticed that small shift to higher diffraction angle (2$\theta$) was carried out in case of thin film. This shift to the higher angle caused due to the stress, strain, dislocation and defects induced since the synthesis parameters and fabrication of [OPDDH]$^{c}$ thin film from solution by using spin coating (SPIN TC100). The effect of DMF solvent in spin coating method (synthesis parameters) might alter the lattice parameters, which may affect the internal

properties of the crystal. The peak position shifted towards to higher angle depend on the internal properties of the crystal.

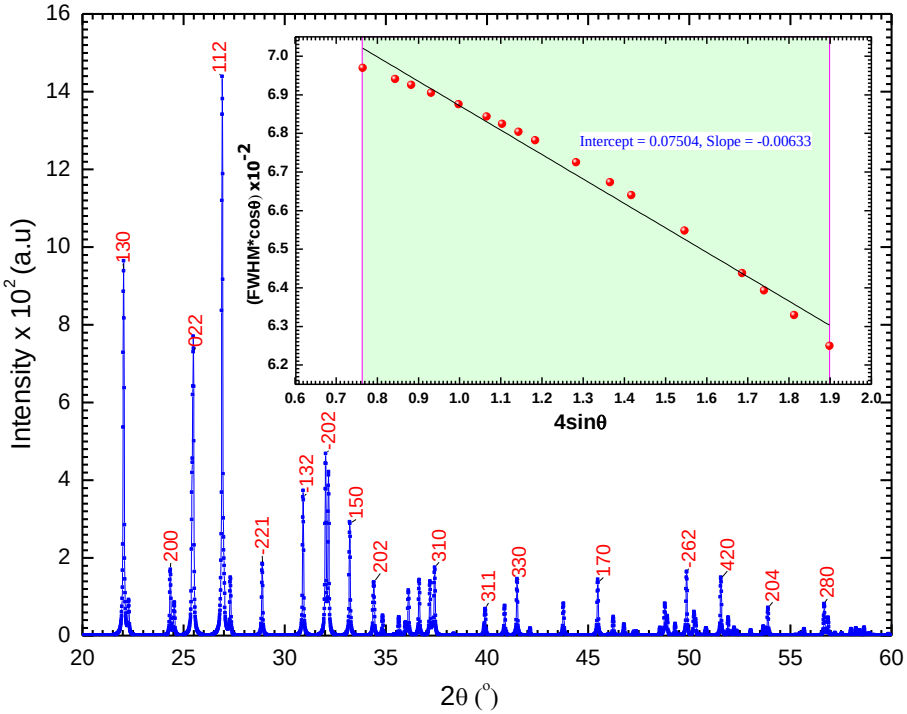


Fig. 10. XRD patterns of the [OPDDH]$^c$ as-deposited thin film.

Table 6. Peak position (2θ), miller indices (hk*l*), FWHM, d-spacing, crystalline size (D), the lattice strain (ε), the dislocation density (δ) and the average inter-crystallite separation (S) of [OPDDH]$^c$ thin film

| No | | Hkl | Int. % | 2θ deg | FWHM | D (nm) | d (Å) | ε x10$^{-3}$ | δ (nm) 10$^{-5}$ | S |
|---|---|---|---|---|---|---|---|---|---|---|
| 1 | Peak Type Gaussian | 130 | 67.4 | 22.036 | 0.071 | 114.087 | 4.03 | 9.116 | 7.683 | 5.036 |
| 2 | | 200 | 11.57 | 24.346 | 0.071 | 114.560 | 3.65 | 8.228 | 7.620 | 4.565 |
| 3 | | 22 | 50.4 | 25.483 | 0.071 | 114.811 | 3.49 | 7.850 | 7.586 | 4.364 |
| 4 | | 112 | 100 | 26.914 | 0.071 | 115.145 | 3.31 | 7.418 | 7.542 | 4.136 |
| 5 | | 221 | 13.04 | 28.89 | 0.071 | 115.640 | 3.09 | 6.891 | 7.478 | 3.858 |
| 6 | | 132 | 26.04 | 30.91 | 0.071 | 116.185 | 2.89 | 6.420 | 7.408 | 3.612 |
| 7 | | 202 | 31.87 | 32.021 | 0.071 | 116.503 | 2.79 | 6.186 | 7.368 | 3.490 |
| 8 | | 150 | 20.57 | 33.22 | 0.071 | 116.860 | 2.69 | 5.950 | 7.328 | 3.367 |
| 9 | | 202 | 5.36 | 34.42 | 0.071 | 117.233 | 2.6 | 5.731 | 7.276 | 3.253 |
| 10 | | 310 | 12.13 | 37.41 | 0.071 | 118.228 | 2.4 | 5.243 | 7.154 | 3.001 |
| 11 | | 311 | 4.69 | 39.92 | 0.071 | 119.141 | 2.26 | 4.887 | 7.0449 | 2.820 |
| 12 | | 330 | 10.19 | 41.49 | 0.071 | 119.748 | 2.17 | 4.686 | 6.974 | 2.717 |
| 13 | | 170 | 0.71 | 45.49 | 0.071 | 121.427 | 1.99 | 4.234 | 6.782 | 2.489 |
| 14 | | 262 | 11.22 | 49.87 | 0.071 | 123.495 | 1.83 | 3.818 | 6.557 | 2.283 |
| 15 | | 420 | 2.18 | 51.56 | 0.071 | 124.362 | 1.77 | 3.675 | 6.466 | 2.213 |
| 16 | | 204 | 5.06 | 53.89 | 0.071 | 125.621 | 1.7 | 3.492 | 6.337 | 2.124 |

| | | | | | | | | | |
|---|---|---|---|---|---|---|---|---|---|
| 17 | 280 | 2.56 | 56.66 | 0.071 | 127.221 | 1.62 | 3.292 | 6.178 | 2.028 |
| Av. | | | | 0.071 | 118.839 | 2.60 | 5.713 | 7.105 | 3.256 |

### 3.6.2. Determination of $E_g^{Opt}$ of [OPDDH]$^c$ thin film

The recorded values of the important absorption edge in the UV region are very suitable for the analysis of the optical transitions and electronic band structure in crystalline or even non-crystalline substances (Fig. 11). The recorded values of absorbance (Abs.) and reflectance (R) of [OPDDH]c thin film were used to estimate the transmittance (T) values using the following equations [39]:

$$T\% = [((1-R)^2 * EXP(-Abs.)) * 100] \quad (3)$$

The dependence of T% and R% of the studied thin film depending on the wavelength (λ) are depicted in Fig. 11. The nanostructured [OPDDH]$^c$ thin film shows T ≅ 73- 94% in most of the visible region of the spectrum. The transmittance increases within the range of 250–650 nm. This indicates a good purity and miscibility between [OPDDH]$^c$ solute and DMF as a solvent. On the other hand, the reflectance (R) spectrum shows an opposite trend with T% within the range of 250 – 650 nm. The reflectance (R%) contains two different absorption bands; the first band appearing as short broad band around 250 nm, while the second band appeared as high broad band at 500 nm. These absorption bands at 250 and 500 nm can be attributed to the electronic transitions consisting of n→π* and π →π*, respectively [40].

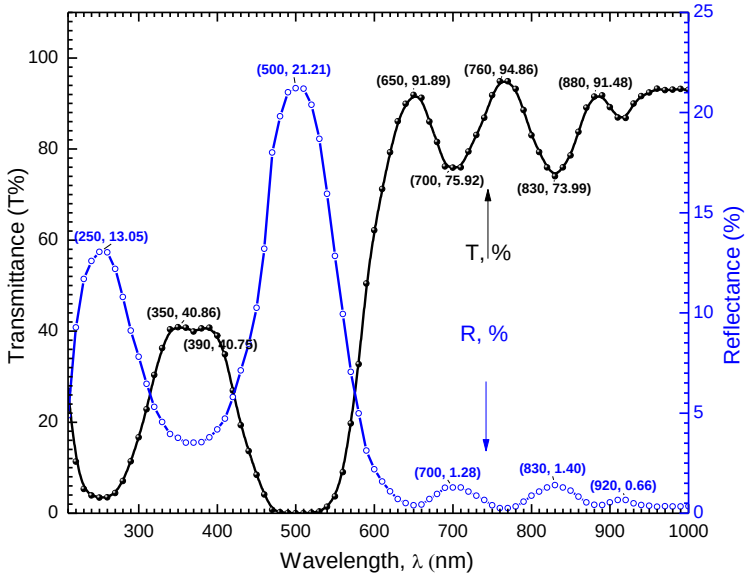


Fig. 11. UV–Visible T% and R% spectra of [OPDDH]$^c$ thin film

The $E_g^{Opt}$ values of the [OPDDH]$^c$ thin film have been calculated using Tauc's formula:

$$[(\alpha h\nu)^A = B(h\nu - E_g^{Opt})] \quad (4)$$

where (hυ) is the energy of incident photons. The absorption coefficient (α) has been obtained via the expression α= the recorded absorption (Abs.) / film thickness (d).

Fig. 12(a, b) represents the linear dependence of both $(\alpha h\nu)^{1/2}$ and $(\alpha h\nu)^2$ on (hυ) at higher photon energies; subsequently the straight-lines are extrapolated both direct and indirect optical transitions have been achieved for this film. The straight-line are extrapolated to zero to give, $E_g^{Opt}$ (Indirect) and $E_g^{Opt}$ (direct). As seen from Fig. 12(a-b), $E_g^{Opt}$ (indirect) of the [OPDDH]$^c$ thin film are 1.96 and 2.79 eV. The same behavior is also observed for $E_g^{Opt}$ (Direct) equal to 2.10 and 3.89 eV of the [OPDDH]$^c$ thin film.

The refractive index, n, is given by the following equation: $n = \left[(1 + R/1 - R) + \sqrt{(4R/(1-R)^2 - k^2}\right]$[41]:, where R is the recorded reflectance and k = αλ/4π is the absorption index.

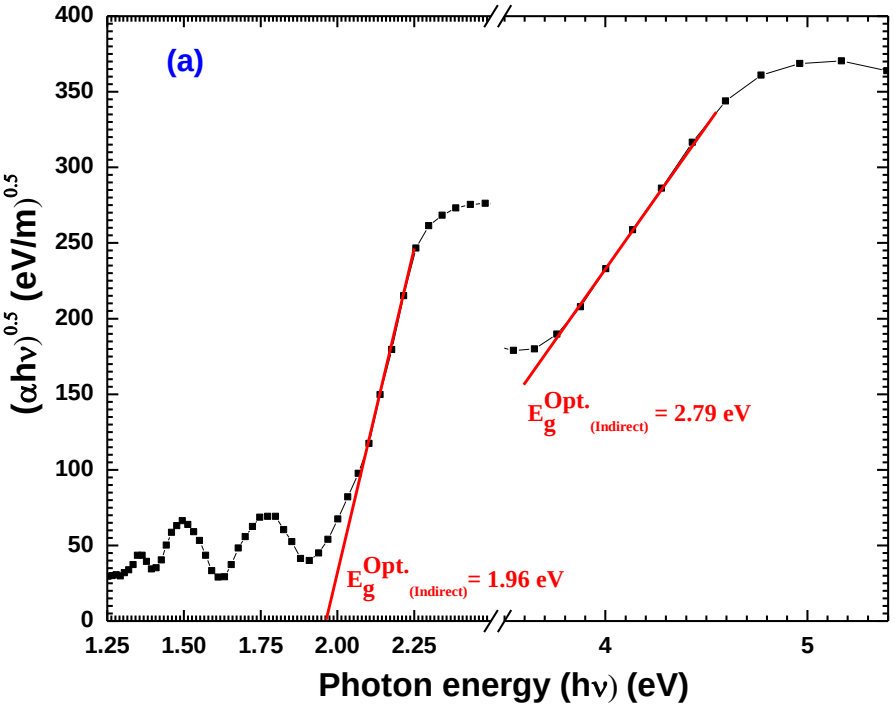

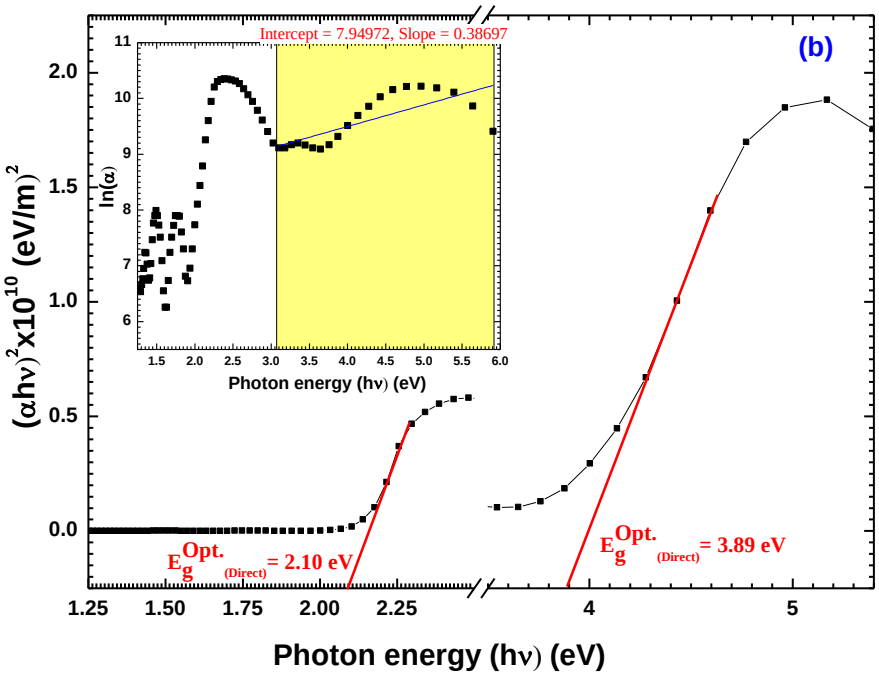


Fig. 12(a-b). (a) The allowed indirect and (b) allowed direct band gaps of [OPDDH]$^c$ thin film

### 3.6.3. Calculation k and n indices of [OPDDH]c thin film

Fig. 13 shows the dependence of k and n of the OPDDH]$^c$ films on the photon energy (hν). The n and k values were found to be 2.48 and 4.77 eV respectively and listed in Table 7. The values of k and n increase from (0.01 to 0.13) and (1.20 to 2.70) with increasing photon energy (1.25 to 2.48), respectively. Moreover, k and n of the [OPDDH]$^c$ thin film decrease very rapidly with increasing photon energy in the range 2.48-3.42eV, and then increase slightly with increasing photon energy in the range 3.42- 4.77eV. It has been established that when the incident light interacts with a nanostructure, thin film has a great quantity of particles, and the refractivity of the films will be increased [42].

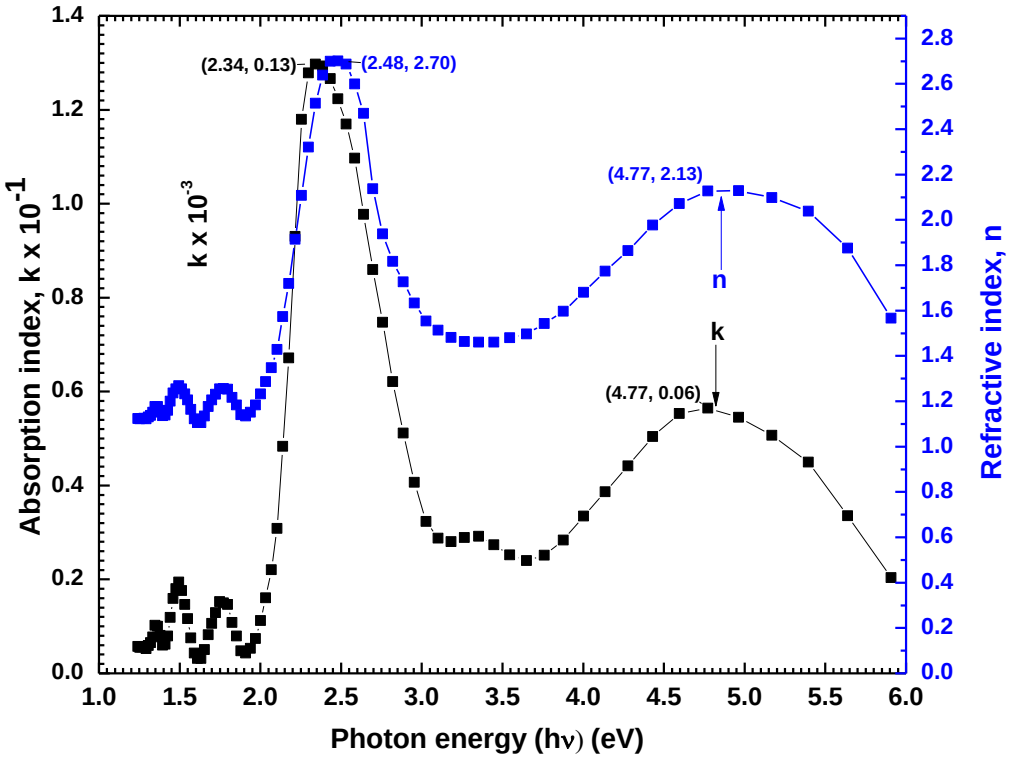


Fig. 13. Absorption index (k) and reflective index (n) as a function of photon energy (hν) of [OPDDH]$^c$ thin film.

Table 7. The direct $E_g^{Opt}$(Direct), indirect $E_g^{Opt}$(Indirect) optical band gap, Urbach energy (EU) and absorption index (k) and the refractive index (n) of the [OPDDH]$^c$ thin films

| Film | $E_g^{Opt}$(Direct)(eV) | | $E_g^{Opt}$(Direct)(eV) | | EU (eV) | k | | n | |
|---|---|---|---|---|---|---|---|---|---|
| | | | | | | 2.34 eV | 4.77 eV | 2.48 eV | 4.77 eV |
| [OPDDH]$^c$ | 1.96 | 2.79 | 2.10 | 3.89 | 0.387 | 0.13 | 0.06 | 2.70 | 2.13 |

The Urbach energy ($E_U$) corresponding to the width of the peak tails for the centered states in $E_g^{Opt}$ were explained by $\alpha = \alpha_o e^{h\nu/E_U}$, where $\alpha_o$ is a constant. The $E_U$ values were estimated from the linear parts of the plot of ln(α) versus hυ, as shown in the inset Fig. 12b. The obtained $E_U$ can be attributed to the disorder in the composition of [OPDDH]$^c$ nanostructure film.

### 3.6.4. Determination of dielectric constant and optical conductivity of [OPDDH]c thin film

The real ($\varepsilon_1$) and imaginary ($\varepsilon_2$) parts of the dielectric constants were determined by the following equations [43]:

$$\varepsilon_1(\omega) = n^2(\omega) - k^2(\omega) \quad (5)$$

$$\varepsilon_2(\omega) = 2n(\omega)k(\omega) \quad (6)$$

The both $\varepsilon_1$ and $\varepsilon_2$ versus hν for [OPDDH]$^c$ thin film were plotted in Fig.14. The variation of the $\varepsilon_1$values part follows the same pattern as the $\varepsilon_2$ part. Obviously, the values of real part are higher than those of the imaginary part. The $\varepsilon_1$ and $\varepsilon_2$ parts of the dielectric constant increase with increasing hν. At photon energies

at 2.43 and 4.77 eV, the values real parts of dielectric constants are 7.28 and 4.53, respectively. Moreover, the values of imaginary parts of dielectric constants are 0.68 and 0.24, respectively.

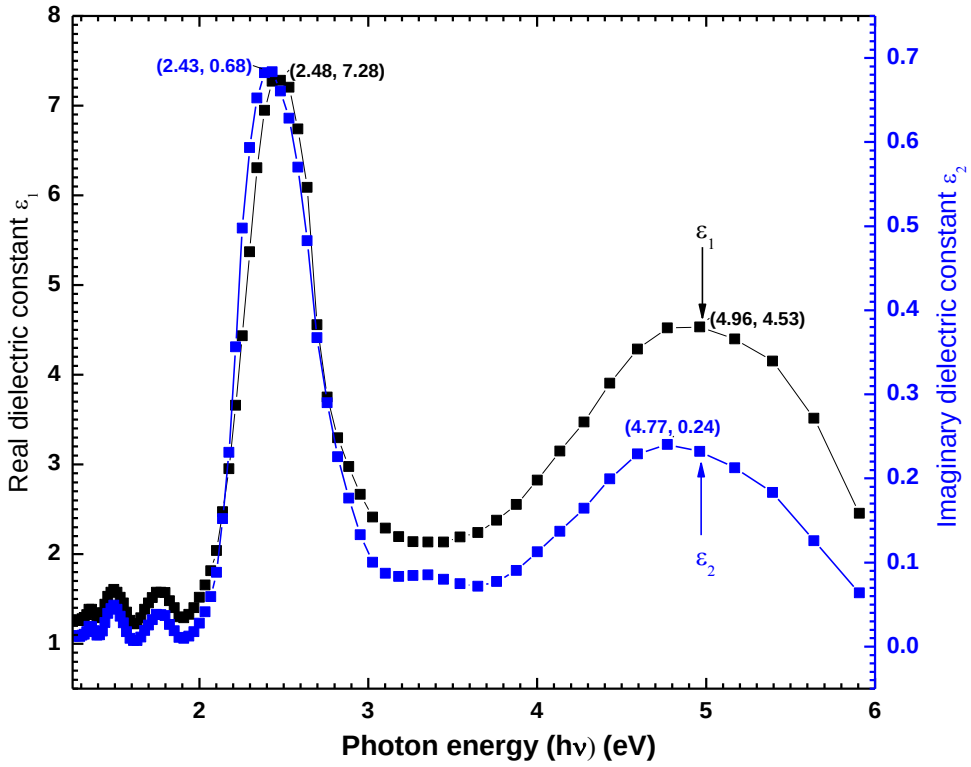


Fig. 14. Plots of $\varepsilon_1$ and $\varepsilon_2$ vs photon energy (hν) of the [OPDDH]$^c$ thin film

The complex optical conductivity $\hat{\sigma} = \sigma_1(\lambda) + i\sigma_2(\lambda)$ is a function of the real and imaginary dielectric constant, expressed by the following relation:

$$\sigma_1 = \omega\varepsilon_2\varepsilon_0 \quad (5)$$

$$\sigma_2 = \omega\varepsilon_1\varepsilon_0 \quad (6)$$

where $\sigma_1$ and $\sigma_2$ are the real and imaginary parts of the optical conductivity. The dependence of both $\sigma_1 and\ \sigma_2$ versus hν for [OPDDH]$^c$ nanostructure thin film (at thickness ≅ 250 nm) are displayed in Fig. 15. The $\sigma_2$ part is higher than the $\sigma_1$. Additionally, both $\sigma_1$ and $\sigma_2$ follow the same behavior for [OPDDH]$^c$ thin film. Fig.15 showed that the presence of two different peaks for $\sigma_1$ and $\sigma_2$ at hν change from 2.00 to 6.00 eV; the source of these peaks may be ascribed to the optical inter band transitions. The maximum obtained values of $\sigma_1 and\ \sigma_2$ depend on nature of [OPDDH]$^c$ thin film. At photon energies at ≅ 2.43 and 5.00 eV, the optical conductivity values of real parts are 223.68 and 154.93 $\Omega^{-1}.cm^{-1}$, respectively. Moreover, the values imaginary parts are 2.43 x$10^3$ and 3.06 x$10^3$ $\Omega^{-1}.cm^{-1}$, respectively.

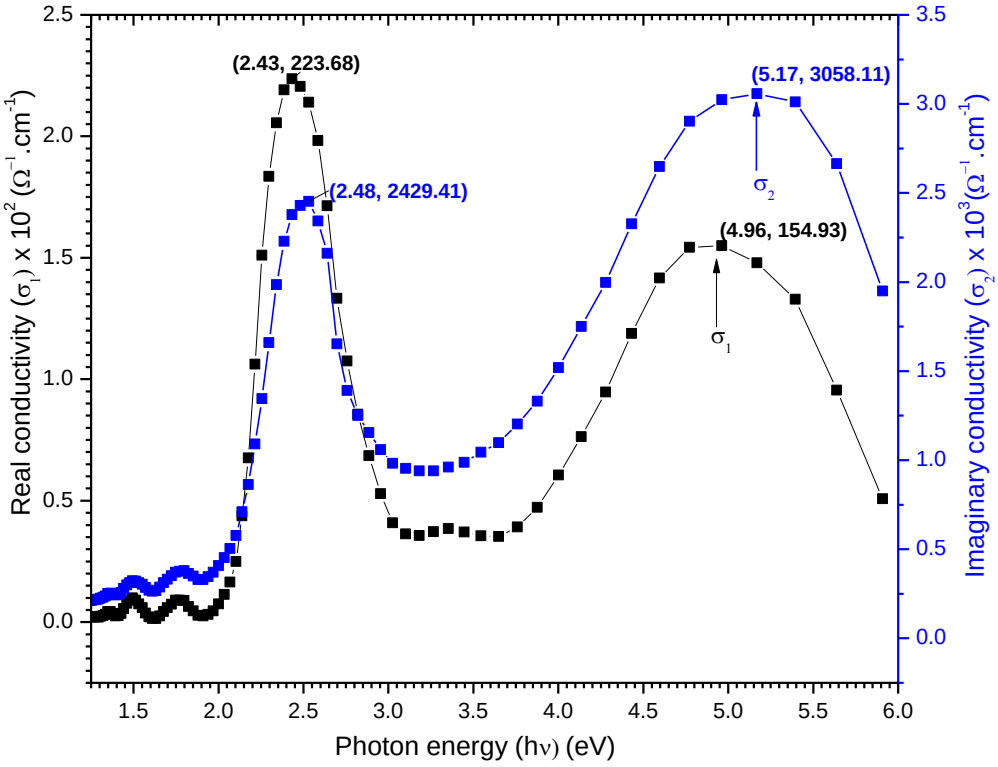


Fig. 15. Plots of $\sigma_1$ and $\sigma_2$ vs photon energy (hν) of the [OPDDH]$^c$ thin film

### 3.6.5. Electrical conductivity of the [OPDDH]c thin film

The dependence of electrical conductivity (σ) of the [OPDDH]$^c$ thin film in the range of 300 K to 398K are shown in Fig. 16. The electrical resistivity (ρ) and σ of the [OPDDH]$^c$ thin film were found to be (400.79 Ω. cm, 2x10$^{-2}$ S. cm$^{-1}$) at 384 k. Designed for [OPDDH]$^c$ polychloride thin film, the obtained conductivity (σ) increases with increasing of the temperature (K). This increasing is attributed to the increase of charge transfer efficacy [44-46]**.** The activation energy ($E_a$) is determined by [47]:

$$\sigma = \sigma_0 \, exp^{\frac{E_a}{kT}} \qquad (9)$$

where $\sigma_0$ is a constant, K is the Boltzmann constant, and Ea is activation energy. The ρ and σ of the [OPDDH]$^c$ thin film necessarily depend on the temperature. The activation energy (Ea) of [OPDDH]$^c$ thin film is found to be 2.01eV. The value of activation energy in lower temperature case is smaller than in higher temperature case. At higher temperature, the electrical conductivity of the [OPDDH]$^c$ thin film is attributed to the thermal excitation of charge carriers from grain boundaries to the neutral region of the nanostructure thin films [47]. In such conditions, the conductivity aspect is produced by the charge carriers' transport to localized states near the conduction band of the [OPDDH]$^c$ thin film

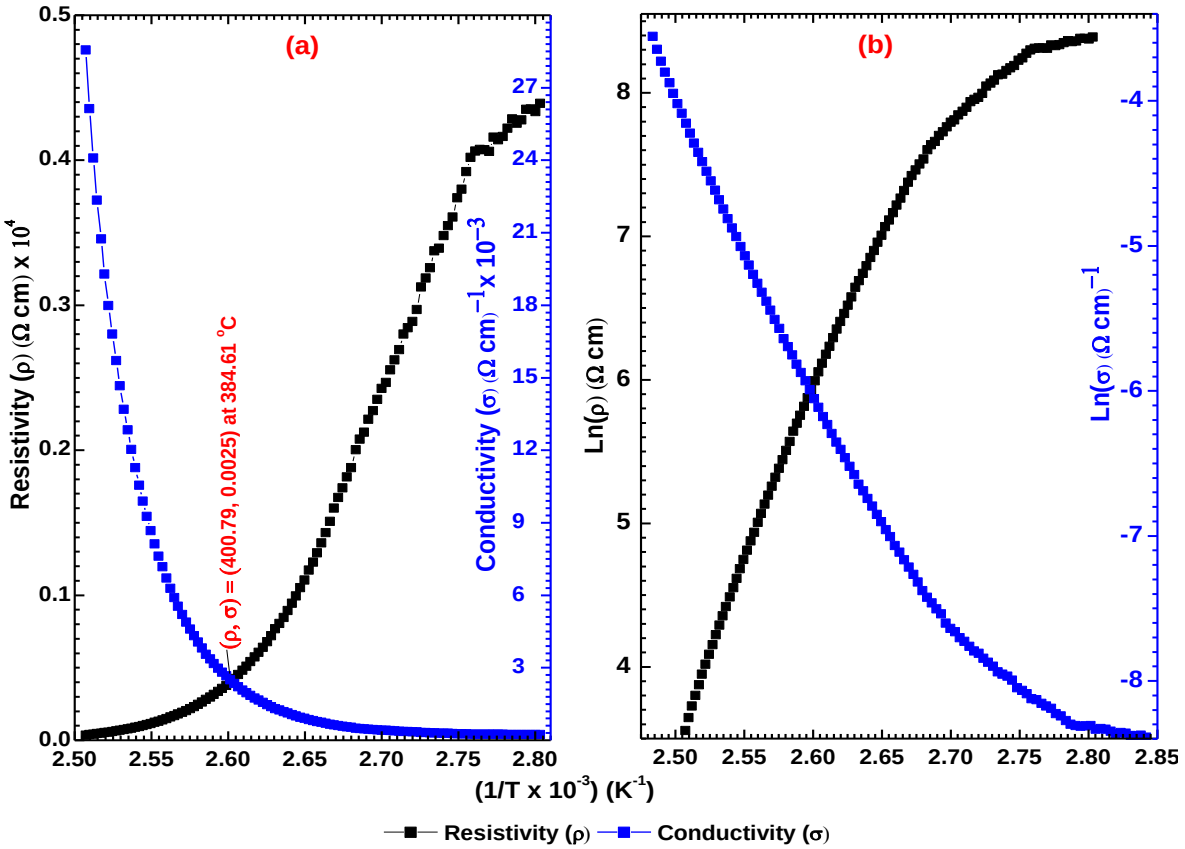


Fig. 16(a-b)**:** Plot of $\rho$ *and* Ln $\sigma$ versus 1/T **of the** [OPDDH]$^{c}$ thin film.

Table 8 displays the obtained electrical conductivity of the [OPDDH]$^{c}$ thin film. These results demonstrate that the [OPDDH]$^{c}$ thin film as a conjugated poly chloride polymer is reliable for application in real optoelectronic devices.

Table (8) Electrical conductivity of the [OPDDH]$^{c}$ thin film under different temperatures.

| Name | Abbreviation | σ (S. cm$^{-1}$) | Polymerization solution | WE$^{(b)}$ | Ref. |
|---|---|---|---|---|---|
| Poly(ortho-phenylenediamine) | | 0.21 | 50 mM oPD$^{(a)}$, 0.1 M $H_2SO_4$ | ITO$^{(c)}$ | [48] |
| | PoPD | $1.2\times10^{-3}$ | 50 mM oPD, 0.1 M $H_2SO_4$ | Pt, Au, ITO | [49] |
| | | $3.1\times10^{-9}$ | 1 mM oPD, 1.5 M HCl | Pt | [50] |
| | | $9.2\times10^{-7}$ | 100 mM oPD, 0.1 M n-$Bu_4NClO_4$/$CH_2ClCH_2Cl$ | Pt (Ni) | [51] |
| *o*-phenylenediamine dihydrochloride | [OPDDH]$^{c}$ | $2\times10^{-2}$ | Spin coating solution | - | Present work |

$^{(a)}$ ortho-phenylene diamine; $^{(b)}$ Working Electrode; $^{(c)}$ Indium tin oxide

## 4. Conclusions

Single Crystal of o-phenylenediamine polychloride, $C_6H_4(NH_2)_2.2HCl$ [OPDDH]$^{c}$ has been successfully synthesized in a highly acidic medium; crystal structure is determined as monoclinic, space group C2/c, with a=7.324(2), b= 14.497 (5), c=7.992(3)Å, α= 90, β= 94.04(4) and γ = 90 (°), V = 846.4(5) Å$^3$ and Z=4. Based

on Hirshfeld surface analysis, Cl…H / H…Cl contacts strongly (55%) to the total HS. The spike at (de + di) ~ 2, 1 Å in acceptor region of FP with a 33%, corresponds to Cl…H contacts. In the donor region, the FP plot matches a 22% contribution from H…Cl contacts to the HS. These Cl…H / H… Cl contacts form a hydrogen bonding 3D supramolecular network in the crystal structure of $[OPDDH]^c$. The H…H interactions appeared in the 2D fingerprint map at the middle of scattered points, including 30.2% of the total Hirshfeld surfaces. The HOMO, LUMO and other active parameters of single crystal are calculated by density functional theory (DFT) on Material Studio 7.0. The refractive parameter dispersion and dielectric constants of $[OPDDH]^c$ are examined by Wemple–DiDomenico and single Sellmeier oscillator models. The optical parameters indicate that the $[OPDDH]^c$ thin film has a comparatively high absorption zone within 2-6 eV photon energy range. The activation energies ($E_a$) and Urbach energy ($E_U$) of $[OPDDH]^c$ thin film are found to be 2.01 and 0.378 eV, respectively. The acquired results indicate that the $[OPDDH]^c$ thin film is a suitable candidate for solar cell based on its dispersion parameters and band gap.

## 5. Supplementary data

**CCDC 1857422** contains the supplementary crystallographic data for $[OPDDH]^c$. These data can be obtained free of charge from The Cambridge Crystallographic Data Centre via https://www.ccdc.cam.ac.uk/structures/Search?access=referee&ccdc=1857422&Author=M.+Sh.+Zoromba

## References


1. Masse, R. & Zyss, J. (1991). *Mol Eng* **1**, 141-152.
2. Kotler, Z., Hierle, R., Josse, D., Zyss, J. & Masse, R. (1992). *JOSA B.* **9**, 534-547.
3. Marder, S. R., Perry, J. W. & Yakymyshyn, C. P. (1994). *Chem mater* **6**, 1137-1147.
4. Vijayalakshmi, A., Vidyavathy, B. & Vinitha, G. (2016). *Ukr J Phy Opt* 98-104.
5. Pal, T., Kar, T., Bocelli, G. & Rigi, L. (2004). *Cryst Growth Des* **4**, 743-747.
6. Rajkumar, R. & Kumar, P. P. (2018). *J Opt* **47**, 75-82.
7. Choubey, A., Kwon, O.-P., Jazbinsek, M. & Günter, P. (2007). *Cryst Growth Des* **7**, 402-405.
8. Stålhandske, C. (1974). *Acta Crystall B-Stru* **30**, 1586-1589.
9. Arora, S., Sundaralingam, M., Dancz, J., Stanford, R. & Marsh, R. (1973). *Acta Crystall B-Stru* **29**, 1849-1855.
10. Hamilton, W. C. (1968). *Methods of Molecular Structure Determination Frontiers in Chemistry*.
11. Mouhat, F. & Coudert, F.-X. (2014). *Phys Rev B* **90**, 224104.
12. Boultif, A. & Louër, D. (1991). *J Appl Crystallogr* **24**, 987-993.
13. Biju, V., Sugathan, N., Vrinda, V. & Salini, S. (2008). *J Mater Sci* **43**, 1175-1179.
14. Zak, A. K., Majid, W. A., Abrishami, M. E. & Yousefi, R. (2011). *Solid State Sci* **13**, 251-256.
15. Delley, B. (1990). *J Chem Phys* **92**, 508-517.
16. Delley, B. (2000). *J Chem Phys* **113**, 7756-7764.
17. Schubert, M. F., Chhajed, S., Kim, J. K., Schubert, E. F., Koleske, D. D., Crawford, M. H., Lee, S. R., Fischer, A. J., Thaler, G. & Banas, M. A. (2007). *Appl Phys Lett* **91**, 231114.
18. Kundu, P. P., Biswas, J., Kim, H. & Choe, S. (2003). *Eur Polym J* **39**, 1585-1593.
19. Domenicano, A., Serantoni, E. F. & Riva di Sanseverino, L. (1977). *Acta Crystall B-Stru* **33**, 1664-1668.

20. Attia, G. & El-Kader, M. A. (2013). *Int J Electrochem Sci* **8**, 5672-5687.
21. Zoromba, M. S., Al-Hossainy, A. & Abdel-Aziz, M. (2017). *Synthetic Met* **231**, 34-43.
22. El Sayed, A. & Morsi, W. (2013). *Polym Composite* **34**, 2031-2039.
23. Rossi, M., Marzilli, L. & Kistenmacher, T. (1978). *Acta Crystall B-Stru* **34**, 2030-2033.
24. Lee, W. E. & Richardson, M. F. (1976). *Can J Chem* **54**, 3001-3006.
25. McKinnon, J. J., Jayatilaka, D. & Spackman, M. A. (2007). *Chem Commun* 3814-3816.
26. El-Gammal, O. A., Al-Hossainy, A. F. & El-Brashy, S. A. (2018). *J Mol Struct* **1165**, 177-195.
27. Matsunaga, T., Hieda, K. & Nikaido, O. (1991). *Photochem Photobiol* **54**, 403-410.
28. Badr, A., El-Amin, A. & Al-Hossainy, A. (2008). *J Phys Chem C* **112**, 14188-14195.
29. Tauc, J., Grigorovici, R. & Vancu, A. (1966). germanium, *Phys Status Solidi (b).* **15**, 627-637.
30. Yang, H., Ge, Y.-Q., Jia, J. & Wang, J.-W. (2011). *J Lumin* **131**, 749-755.
31. Badr, A., El-Amin, A. & Al-Hossainy, A. (2006). *Eur Phys J B* **53**, 439-448.
32. Stålhandske, C. (1974). *Acta Crystall B-Stru* **30**, 1586-1589.
33. Orlandi, P., Biagioni, C., Moëlo, Y., Bonaccorsi, E. & Paar, W. H. (2013). *Can Mineral* **51**, 475-494.
34. Boultif, A. & Louër, D. (1991). *J Appl Crystallogr* **24**, 987-993.
35. Biju, V., Sugathan, N., Vrinda, V. & Salini, S. (2008). *J Mater Sci* **43**, 1175-1179.
36. Zak, A. K., Majid, W. A., Abrishami, M. E. & Yousefi, R. (2011). *Solid State Sci* **13**, 251-256.
37. Schubert, M. F., Chhajed, S., Kim, J. K., Schubert, E. F., Koleske, D. D., Crawford, M. H., Lee, S. R., Fischer, A. J., Thaler, G. & Banas, M. A. (2007). *Appl Phys Lett* **91**, 231114.
38. Kundu, P. P., Biswas, J., Kim, H. & Choe, S. (2003). *Eur Polym J* **39**, 1585-1593.
39. Ali, A., Ammar, A. & Moez, A. A. (2014). *Superlattice Microstr* **65**, 285-298.
40. Attia, G. & El-Kader, M. A. (2013). *Int J Electrochem Sci.* **8**, 5672-5687.
41. Al-Hossainy, A. & Zoromba, M. S. (2019). *J Alloy Comp* **789**, 670-680.
42. Al-Hossainy, A. F. (2016). *B Mater Sci* **39**, 209-222.
43. Ibrahim, A., Abdel-Aziz, M., Zoromba, M. S. & Al-Hossainy, A. (2018). *Synthetic Met* **238**, 1-13.
44. Leclerc, M., D'Aprano, G. & Zotti, G. (1993). *Synthetic Met* **55**, 1527-1532.
45. Zuo, F., Angelopoulos, M., MacDiarmid, A. G. & Epstein, A. J. (1987). *Phys Rev B* **36**, 3475.
46. Chougule, M. A., Pawar, S. G., Godse, P. R., Mulik, R. N., Sen, S. & Patil, V. B. (2011). *Soft Nanosci Lett* **1**, 6.
47. Zhao, Z., Morel, D. & Ferekides, C. (2002). Thin Solid Films. 413, 203-211.
48. Ogura, K., Kokura, M., Yano, J. & Shiigi, H. (1995). Electrochim Acta. 40, 2707-2714.
49. Yano, J. (1995). J Polym Sci A1 33, 2435-2441.
50. McEvoy, T. M., Long, J. W., Smith, T. J. & Stevenson, K. J. (2006). Langmuir. 22, 4462-4466.
51. Li, X.-G., Huang, M.-R., Duan, W. & Yang, Y.-L. (2002). Chem Rev 102, 2925-3030.